

RECEIVED: January 19, 2022

REVISED: April 20, 2022

ACCEPTED: May 5, 2022

PUBLISHED: June 13, 2022

Quasinormal modes of black holes with multiple photon spheres

Guangzhou Guo,^a Peng Wang,^a Houwen Wu^{a,b} and Haitang Yang^a

^aCenter for Theoretical Physics, College of Physics, Sichuan University, Chengdu, 610064, China

^bDepartment of Applied Mathematics and Theoretical Physics, University of Cambridge, Wilberforce Road, Cambridge, CB3 0WA, U.K.

E-mail: gzguo@stu.scu.edu.cn, pengw@scu.edu.cn, hw598@damtp.cam.ac.uk, hyanga@scu.edu.cn

ABSTRACT: For a static and spherically symmetric black hole, a photon sphere is composed of circular null geodesics of fixed radius, and plays an important role in observing the black hole. Recently, in an Einstein-Maxwell-scalar model with a non-minimal coupling between the scalar and electromagnetic fields, a class of hairy black holes has been found to possess two unstable and one stable circular null geodesics on the equatorial plane, corresponding to three photon spheres outside the event horizon. In this paper, we study quasinormal modes of the scalar field, which are associated with these circular null geodesics, in the hairy black hole spacetime. In the eikonal regime with $l \gg 1$, the real part of the quasinormal modes is determined by the angular velocity of the corresponding circular geodesics. The imaginary part of the quasinormal modes associated with the unstable circular null geodesics encodes the information about the Lyapunov exponent of the corresponding circular geodesics. Interestingly, we find long-lived and sub-long-lived modes, which are associated with the stable and one of the unstable circular null geodesics, respectively. Due to tunneling through potential barriers, the damping times of the long-lived and sub-long-lived modes can be exponentially and logarithmically large in terms of l , respectively.

KEYWORDS: Black Holes, Classical Theories of Gravity

ARXIV EPRINT: [2112.14133v2](https://arxiv.org/abs/2112.14133v2)

Contents

1	Introduction	1
2	Hairy black holes	3
2.1	Black hole solution	3
2.2	Circular null geodesics	4
2.3	Lyapunov exponent	5
3	Quasinormal modes	6
3.1	Modes at global maximum	8
3.2	Long-lived modes at minimum	9
3.3	Sub-long-lived modes at local maximum	12
4	Conclusions	16
A	Derivations of eqs. (3.17) and (3.19)	18

1 Introduction

In the last decade, gravitational waves from a binary black hole merger were successfully detected by LIGO and Virgo [1], and subsequently the first image of a supermassive black hole at the center of galaxy M87 was photographed by the Event Horizon Telescope (EHT) [2–7], which opens a new era of black hole physics. Due to the event horizon, a black hole is a dissipative system, eigenmodes of which are quasinormal modes. The final stage of a binary black hole merger is ringdown, in which the gravitational waveforms are described by a superposition of quasinormal modes [8]. Quasinormal modes with complex frequencies have vast applications in black hole physics [9–20]. In particular, a linear perturbation can induce a discrete set of quasinormal modes, whose imaginary part is related to the damping time scale. The spectrum of quasinormal modes therefore provides a perspective on the study of stability of the background spacetime [21–26]. Moreover, the most dominant quasinormal modes can be used to check the validity of the strong cosmic censorship conjecture [27–29].

Since exotic horizonless objects, e.g., wormholes and ultra-compact objects (UCOs), have optical observations similar to black holes, they have recently attracted great attention [30–37]. Interestingly, a reflecting boundary in the wormhole or UCO spacetime can produce a set of time-delay echoes, which are characterized by quasinormal modes [38–41]. Furthermore, UCOs have been conjectured to suffer from instabilities due to the existence of a family of long-lived quasinormal modes, which appear in the neighborhood of a stable circular null geodesic [42–44]. For instance, a linear ergoregion instability associated with long-lived modes may occur for a spinning object with a sufficiently high rotation speed [45–47].

Intriguingly, unstable null geodesics have been revealed to be closely related to a class of quasinormal modes of perturbations in the black hole spacetime [9, 10, 16, 48–52]. In [9], null geodesics were first found to be connected with quasinormal modes in Schwarzschild and slowly rotating Kerr black holes. Using the WKB approximation in the eikonal limit, the authors of [48] elaborated the connection in the static, spherically symmetric and asymptotically flat black hole background. To be more specific, it verified that the real part of quasinormal modes is proportional to the angular velocity of the corresponding unstable circular null geodesic, while the imaginary part is determined by the Lyapunov exponent of the orbit. Furthermore, the relation between null geodesics and quasinormal modes was generalized to Kerr black holes of arbitrary spin in [16], which showed an extra precession modification in the real part compared to non-rotating black holes.

The No-hair theorem asserts that a black hole is uniquely determined by its three parameters, i.e., mass, electric charge and angular momentum [53–55]. However, hairy black holes with extra freedom have been constructed in various models, which provide counter-examples to the no-hair theorem [56–62]. Recently, a type of Einstein-Maxwell-scalar (EMS) models with a non-minimal coupling between the scalar and electromagnetic fields have been extensively studied in the literature [23, 26, 63–78]. In the EMS models, the non-minimal coupling destabilizes scalar-free black holes and induce the onset of spontaneous scalarization to form hairy black holes with a scalar hair [63]. In [24, 25, 79], the stability of the hairy black holes was analyzed by calculating their quasinormal modes of various perturbations. Decaying quasinormal modes may suggest that the hairy black holes are the endpoints of the dynamic evolution from unstable scalar-free black hole solutions.

Surprisingly, it showed that in a certain parameter regime of the hairy black holes, there exist two unstable and one stable null circular null geodesics on the equatorial plane, which indicates three photon spheres of different sizes outside the event horizon [76, 77]. Due to a double-peak structure appearing in the potential of the photon radial motion, the existence of two unstable photon spheres can remarkably affect the optical appearance of black holes illuminated by the surrounding accretion disk, e.g., leading to bright rings of different radii in the black hole image [76] and significantly increasing the flux of the observed image [77]. The relation between null geodesics and quasinormal modes has been rarely reported for black holes with more than one photon sphere. Moreover, multiple photon spheres appearing in some spacetime signal the existence of long-live modes, which may render the spacetime unstable [42–44]. Therefore, it is of great interest to study quasinormal modes of the hairy black holes endowed with three photon spheres. Note that multiple photon spheres have recently been reported in different black hole models [80–82].

In this paper, we use the WKB method to calculate quasinormal modes localized at circular null geodesics of the hairy black holes with three photon spheres. The rest of the paper is organized as follows. In section 2, we study null circular geodesics of hairy black holes in the EMS model, as well as the orbital stability by evaluating the Lyapunov exponent. Subsequently, quasinormal modes trapped at different circular null geodesics are obtained in section 3. We conclude our main results in section 4. The appendix A is devoted to derivations of some WKB formulas. We set $16\pi G = 1$ throughout this paper.

2 Hairy black holes

In this section, we first briefly review spherically symmetric hairy black hole solutions in the EMS model. Subsequently, we study circular geodesics for photons around the hairy black holes and compute the corresponding Lyapunov exponents.

2.1 Black hole solution

In the EMS model, the action is given by

$$S = \int d^4x \sqrt{-g} \left[R - 2\partial_\mu \phi \partial^\mu \phi - e^{\alpha\phi^2} F^{\mu\nu} F_{\mu\nu} \right], \quad (2.1)$$

where the scalar field ϕ is minimally coupled to the metric field and non-minimally coupled to the electromagnetic field A_μ . Here, $F_{\mu\nu} = \partial_\mu A_\nu - \partial_\nu A_\mu$ is the electromagnetic field strength tensor, and $e^{\alpha\phi^2}$ is the coupling function between ϕ and A_μ . Following [26, 63], we restrict our attention to static, spherically symmetric and asymptotically flat black hole solutions with the generic ansatz

$$ds^2 = -N(r) e^{-2\delta(r)} dt^2 + \frac{1}{N(r)} dr^2 + r^2 (d\theta^2 + \sin^2 \theta d\varphi^2),$$

$$A_\mu dx^\mu = V(r) dt \text{ and } \phi = \phi(r). \quad (2.2)$$

The equations of motion are then given by

$$N'(r) = \frac{1 - N(r)}{r} - \frac{Q^2}{r^3 e^{\alpha\phi^2(r)}} - rN(r) \phi'^2(r),$$

$$\left[r^2 N(r) \phi'(r) \right]' = -\frac{\alpha\phi(r) Q^2}{e^{\alpha\phi^2(r)} r^2} - r^3 N(r) \phi'^3(r),$$

$$\delta'(r) = -r\phi'^2(r), \quad (2.3)$$

$$V'(r) = \frac{Q}{r^2 e^{\alpha\phi^2(r)}} e^{-\delta(r)},$$

where primes denote derivatives with respect to r , and the integration constant Q is interpreted as the electric charge of the black hole solution.

To find black holes solutions from the non-linear ordinary differential equations (2.3), one needs to impose proper boundary conditions at the event horizon r_h and the spatial infinity,

$$N(r_h) = 0, \delta(r_h) = \delta_0, \phi(r_h) = \phi_0, V(r_h) = 0,$$

$$N(\infty) = 1, \delta(\infty) = 0, \phi(\infty) = 0, V(\infty) = \Phi, \quad (2.4)$$

where Φ is the electrostatic potential. The two parameters δ_0 and ϕ_0 determine the asymptotic behavior of the solutions in the vicinity of the horizon. Moreover, the black hole mass M , which is related to the ADM mass, can be obtained via $M = \lim_{r \rightarrow \infty} r [1 - N(r)] / 2$. In this paper, we set $M = 1$ and use a shooting method to numerically solve eq. (2.3) for black hole solutions matching the boundary conditions (2.4). It is manifest that the scalar-free solutions with $\phi = 0$ (i.e., Reissner-Nordström black holes) can exist in the EMS model. Nevertheless, we focus on hairy black holes with the non-trivial profile of the scalar field ϕ . For instance, we exhibit the profile of the metric functions for the hairy black hole solution with $\alpha = 0.9$ and $Q = 1.066$ in the left panel of figure 1.

2.2 Circular null geodesics

Owing to strong gravity near a black hole, photons are forced to travel in circular null geodesics on photon spheres, which play an important role in determining properties of the black hole image seen by a distant observer (e.g., the size of the black hole shadow). Here, circular null geodesics of the spherically symmetric hairy black hole are studied. Without loss of generality, we consider a photon moving on the equatorial plane with $\theta = \pi/2$. To obtain equatorial geodesics, we start from the Lagrangian

$$\mathcal{L} = \frac{1}{2} \left(-N(r) e^{-2\delta(r)} \dot{t}^2 + \frac{1}{N(r)} \dot{r}^2 + r^2 \dot{\varphi}^2 \right), \quad (2.5)$$

where dots denote derivatives with respect to the affine parameter τ . The generalized canonical momenta for this Lagrangian are defined as

$$\begin{aligned} -p_t &= N(r) e^{-2\delta(r)} \dot{t} = E, \\ p_\varphi &= r^2 \dot{\varphi} = L, \\ p_r &= \frac{1}{N} \dot{r}. \end{aligned} \quad (2.6)$$

Note that the metric of the hairy black hole spacetime is independent of t and φ . So the spacetime admits two Killing vectors, which are associated with the conserved energy E and momentum L , respectively, in eq. (2.6). Varying the Lagrangian (2.5) with respect to r yields the radial equation of motion for the photon,

$$\frac{d}{d\tau} \frac{\partial \mathcal{L}}{\partial \dot{r}} = \frac{\partial \mathcal{L}}{\partial r}. \quad (2.7)$$

With the help of eq. (2.6), eq. (2.7) becomes

$$e^{-2\delta(r)} \dot{r}^2 = E^2 - \frac{e^{-2\delta(r)} N(r)}{r^2} L^2, \quad (2.8)$$

which describes a null geodesic. For later use, one can introduce the geometric potential as

$$V_{\text{geo}}(r) = \frac{e^{-2\delta(r)} N(r)}{r^2}. \quad (2.9)$$

Accordingly, a null circular geodesic at $r = r_c$ can appear, provided that the conditions $V_{\text{geo}}(r_c) = E^2/L^2$ and $V'_{\text{geo}}(r_c) = 0$ are satisfied.

In figure 1, we present the geometric potential for hairy black holes with $\alpha = 0.9$ for $Q = 1.066, 1.064$ and 1.059 in the right panel. When $Q = 1.059$ (the blue line), the geometric potential possesses a single maximum outside the event horizon. Intriguingly for $Q = 1.066$ and 1.064 (the red and orange lines), it displays a double-peak structure with one minimum and two maxima, which implies that there exist three null circular geodesics located at the extrema.

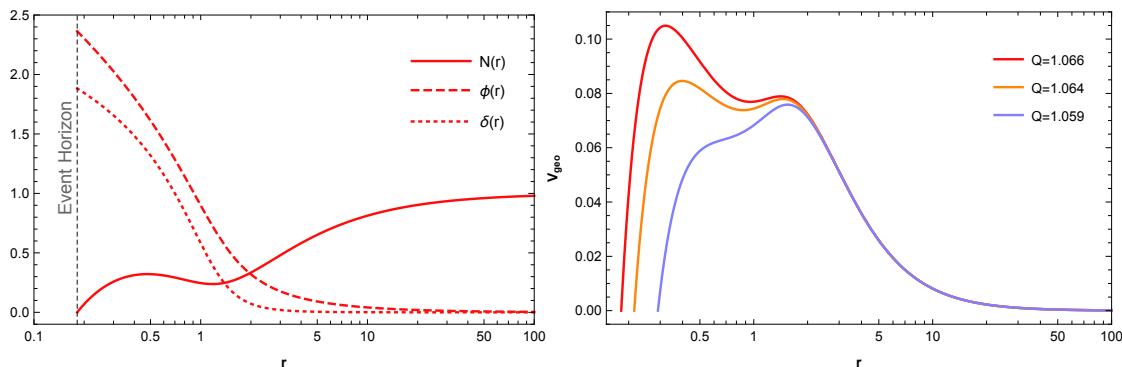


Figure 1. Metric functions and geometric potential for hairy black hole solutions, where we take $\alpha = 0.9$. *Left:* the metric functions $N(r)$ (solid line), $\phi(r)$ (dashed line) and $\delta(r)$ (dotted line) for the hairy black hole solution with $Q = 1.066$ are plotted outside the event horizon (vertical dashed line). *Right:* the geometric potential for different hairy black holes with $Q = 1.066$ (red line), $Q = 1.064$ (orange line) and $Q = 1.059$ (blue line). For a large value of charge (e.g., the red and orange lines), the geometric potential possesses a double-peak structure with one local minimum and two local maxima. By contrast, the double-structure disappears as the charge decreases (e.g., the blue line), leaving only a single maximum of the geometric potential.

2.3 Lyapunov exponent

The Lyapunov exponent is proposed to characterize the rate of separation of adjacent trajectories in the phase space [48, 83]. In a dynamical system, the sign of the Lyapunov exponent can be used to determine whether adjacent trajectories converge or not. Specifically, positive Lyapunov exponents correspond to the divergent trajectories, while negative ones to the convergent trajectories. Therefore, we can study the stability of null circular orbits around a hairy black hole by evaluating their Lyapunov exponents. Moreover, the Lyapunov exponent can be closely related to quasinormal modes of black holes. Indeed, it showed in [48] that, if the geometric potential has a single maximum, the imaginary part of quasinormal modes is determined by the Lyapunov exponent of the unstable circular orbit at the maximum in the eikonal regime.

To describe circular orbits in spherically symmetric spacetime, we focus on a two dimensional phase space spanned by $X_i(t) \equiv (p_r, r)$. The equations of motion in this phase space can be schematically written as

$$\frac{dX_i}{dt} = H_i(X_j). \tag{2.10}$$

To obtain the Lyapunov exponent of a given orbit, we need to linearize eq. (2.10) around the orbit,

$$\frac{d\delta X_i(t)}{dt} = K_{ij}(t) \delta X_j(t), \tag{2.11}$$

where the linear stability matrix $K_{ij}(t)$ is

$$K_{ij}(t) = \left. \frac{\partial H_i}{\partial X_j} \right|_{X_i(t)} = \begin{pmatrix} 0 & d(t^{-1} \dot{p}_r) / dr \\ t^{-1} N & 0 \end{pmatrix}. \tag{2.12}$$

The solution to the linearized equation (2.11) can be expressed as

$$\delta X_i(t) = L_{ij}(t) \delta X_j(0), \quad (2.13)$$

where the evolution matrix $L_{ij}(t)$ satisfies

$$\frac{dL_{ij}(t)}{dt} = K_{im}(t) L_{mj}(t), \quad (2.14)$$

and $L_{ij}(0) = \delta_{ij}$. The principal Lyapunov exponent is related to the determination of the eigenvalues of L_{ij} , i.e.,

$$\lambda = \lim_{t \rightarrow \infty} \frac{1}{t} \log \frac{L_{jj}(t)}{L_{jj}(0)}. \quad (2.15)$$

From eq. (2.12), the principal Lyapunov exponent can be written as

$$\lambda = \pm \sqrt{t^{-1} N \frac{d}{dr} (t^{-1} p_r)}, \quad (2.16)$$

where we choose the + sign for the Lyapunov exponent [48]. Specifically, the Lyapunov exponent of a circular orbit at $r = r_c$ can be expressed in terms of the geometric potential,

$$\lambda|_{r=r_c} = \sqrt{-\frac{L^2 e^{2\delta}}{2\dot{t}^2} V''_{\text{geo}}}\Big|_{r=r_c} = \sqrt{-\frac{1}{2V_{\text{geo}}} \frac{d^2}{dx^2} V_{\text{geo}}}\Big|_{r=r_c}, \quad (2.17)$$

where the tortoise coordinate x is defined by $dx/dr \equiv e^{\delta(r)} N^{-1}(r)$. For a circular null orbit located at a local maximum of the geometric potential with $V''_{\text{geo}} < 0$, the Lyapunov exponent λ is positive, which implies that the orbit is unstable under small perturbations. On the other hand, a circular orbit located at a local minimum has $V''_{\text{geo}} > 0$ and hence has a purely imaginary value of the Lyapunov exponent, which implies that the orbit is stable. Therefore, a black hole with a double-peak geometric potential (e.g., $Q = 1.066$ and 1.064 in figure 1) has two unstable circular null geodesics at the local maxima and a stable one at the local minimum. In addition, we introduce the angular velocity Ω of the circular orbit at $r = r_c$ via

$$\Omega|_{r=r_c} = \frac{\dot{\phi}}{\dot{t}}\Big|_{r=r_c} = \sqrt{V_{\text{geo}}}\Big|_{r=r_c}, \quad (2.18)$$

which can be related to the real part of quasinormal modes [48].

3 Quasinormal modes

In this section, we consider the perturbation of the scalar field and compute its quasinormal modes that are associated with the circular null geodesics in the hairy black hole background (2.2). For a scalar perturbation of mode

$$\delta\phi = e^{-i\omega t} \frac{\Psi_{\omega l}(r) Y_{lm}(\theta, \phi)}{r}, \quad (3.1)$$

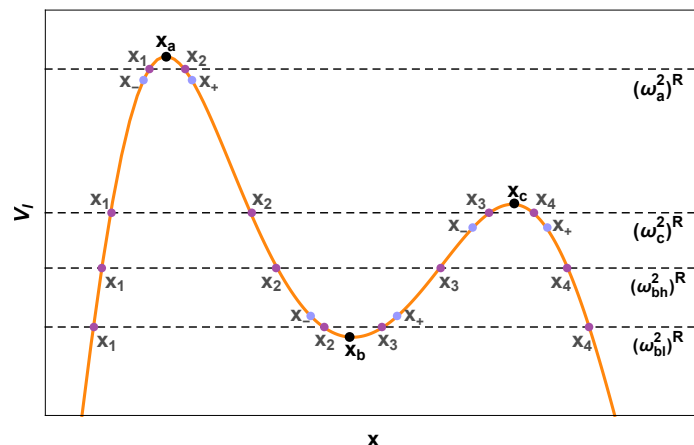


Figure 2. The effective potential V_l as a function of the tortoise coordinate x . Here we present a local region of the effective potential for the hairy black hole with $\alpha = 0.9$ and $Q = 1.066$. Note that the effective potential tends to vanish as $x \rightarrow \pm\infty$. The horizontal dashed lines represent the real parts of quasinormal modes ω^2 in different cases, which intersect the effective potential at the turning points labelled by x_1, x_2, x_3 and x_4 . The black points denote the extrema of V_l at x_a, x_b and x_c , respectively, which correspond to the circular null geodesics in the eikonal limit. Around the extrema, the effective potential can be approximated by a parabola between the blue points x_- and x_+ .

we can separate the angular variables and express the linearized equation for $\Psi_{\omega l}(r)$ in the following general form,

$$\left(\frac{d^2}{dx^2} + \omega^2 - V_l(r) \right) \Psi_{\omega l}(r) = 0, \quad (3.2)$$

where the effective potential is

$$V_l(r) = \frac{e^{-2\delta(r)} N(r)}{r^2} \left[l(l+1) + 1 - N(r) - \frac{Q^2}{r^2 e^{\alpha\phi(r)^2}} - \left(\alpha + 2\alpha^2\phi(r)^2 \right) \frac{Q^2}{r^2 e^{\alpha\phi(r)^2}} \right]. \quad (3.3)$$

In the eikonal regime ($l \gg 1$), the effective potential reduces to

$$V_l(r) \simeq l^2 \frac{e^{-2\delta(r)} N(r)}{r^2} = l^2 V_{\text{geo}}(r), \quad (3.4)$$

where $V_{\text{geo}}(r)$ is the aforementioned geometric potential. It is worth emphasizing that the full perturbed fields around the hairy black hole background were considered in [24]. In particular, eq. (41) of [24] describes the scalar perturbation propagating in the hairy black holes. In the eikonal limit with $l \rightarrow \infty$, keeping only the $\mathcal{O}(l^2)$ leading terms in the right-hand side of eq. (41) would reduce eq. (41) to eq. (3.2) with the effective potential (3.4). Note that the terms coupling the gravitational and electromagnetic sectors with the scalar perturbation are the order of l and hence are subleading in the eikonal limit.

In figure 2, we plot the effective potential V_l with $l = 3$ for the hairy black hole solution with $\alpha = 0.9$ and $Q = 1.066$. Like the geometric potential, V_l displays a double-peak structure, i.e., two local maxima and one minimum. The effective potential V_l with $l > 3$ is

found to have a similar profile. Since quasinormal modes are determined by the effective potential V_l , multiple local extrema of V_l could lead to distinct types of quasinormal modes. In the rest of the section, we apply the WKB approximation to studying quasinormal modes trapped at the extrema of the effective potential with a double-peak structure. These modes can be interpreted as photons moving in the circular null geodesics determined by $V_{\text{geo}}(r)$, which leak out slowly. Since we are interested in the large l limit, the WKB approximation can be accurate enough for computing quasinormal modes. Note that quasinormal modes occur only when appropriate boundary conditions are imposed, i.e., purely ingoing modes at $x = -\infty$ (at the event horizon) and purely outgoing modes at $x = +\infty$ (at the spatial infinity),

$$\begin{aligned} \Psi_{\omega l} &\sim e^{-i\omega x}, & \text{when } x = -\infty, \\ \Psi_{\omega l} &\sim e^{i\omega x}, & \text{when } x = +\infty. \end{aligned} \tag{3.5}$$

For comparison, we perform a direct integration to numerically solve eq. (3.2) to obtain exact quasinormal modes of interest for hairy black holes [24, 42]. To accurately extract exact modes, we use the NDSolve function built in the Wolfram Mathematica to search for quasinormal modes satisfying the boundary condition (3.5), where the ingoing and outgoing modes are expanded into series up to 14th order near the event horizon and in the far field, respectively. Without causing any ambiguity, we denote the geometric potential, the effective potential and the metric functions with respect to the tortoise coordinate x by $V_{\text{geo}}(x)$, $V_l(x)$, $N(x)$ and $\delta(x)$, respectively.

3.1 Modes at global maximum

We first discuss the quasinormal modes of frequency ω_a trapped at the global maximum of the effective potential at $x = x_a$. For such modes, the $(\omega_a^2)^R$ line lies close to the global maximum and intersects the potential at the turning points x_1 and x_2 , around which the WKB approximation fails. There exists some small positive constant δ such that the WKB approximation is valid for $x < x_1 - \delta$ and $x > x_2 + \delta$. Therefore, the solution of eq. (3.2) can be approximated by the WKB expansions in $(-\infty, x_1 - \delta)$ and $(x_2 + \delta, +\infty)$, which match the ingoing and outgoing boundary conditions, respectively. In the vicinity of $x = x_a$, the potential can be approximated by a parabola. If $(\omega_a^2)^R$ is close enough to the global maximum, there exist x_- and x_+ with $x_- < x_1 - \delta < x_2 + \delta < x_+$, such that the effective potential is well approximated by a parabola for $x_- < x < x_+$ (see figure 2). In (x_-, x_+) , eq. (3.2) with an approximated parabolic potential can be exactly solved in terms of parabolic cylinder functions. Furthermore, a complete solution requires that the two WKB expansions should be smoothly connected by the exact solution in the overlapping regions $(x_-, x_1 - \delta)$ and $(x_2 + \delta, x_+)$. The matching procedure then gives [84]

$$\frac{\omega_a^2 - V_l(x_a)}{\sqrt{-2V_l^{(2)}(x_a)}} = i \left(n + \frac{1}{2} \right) \text{ with } n = 0, 1, 2 \dots, \tag{3.6}$$

where the superscript of $V_l^{(2)}(x_a)$ denotes the second derivative over the tortoise coordinate x .

	Modes at Global Maximum	
	Exact Modes	WKB Modes
$l = 10$	$\pm 3.3627 - 0.09575i$	$\pm 3.3680 - 0.09503i$
$l = 12$	$\pm 4.0166 - 0.09517i$	$\pm 4.0211 - 0.09503i$
$l = 14$	$\pm 4.6689 - 0.09513i$	$\pm 4.6728 - 0.09503i$
$l = 16$	$\pm 5.3202 - 0.09509i$	$\pm 5.3235 - 0.09503i$
$l = 18$	$\pm 5.9706 - 0.09510i$	$\pm 5.9736 - 0.09503i$
$l = 20$	$\pm 6.6206 - 0.09509i$	$\pm 6.6233 - 0.09503i$
$l = 22$	$\pm 7.2701 - 0.09510i$	$\pm 7.2726 - 0.09503i$
$l = 24$	$\pm 7.9194 - 0.09511i$	$\pm 7.9217 - 0.09503i$
$l = 26$	$\pm 8.5685 - 0.09509i$	$\pm 8.5706 - 0.09504i$
$l = 28$	$\pm 9.2174 - 0.09508i$	$\pm 9.2193 - 0.09504i$
$l = 30$	$\pm 9.8661 - 0.09510i$	$\pm 9.8679 - 0.09504i$

Table 1. Lowest-lying quasinormal modes living near the global maximum of the effective potential, which are computed by a numerical method of direct integration and the WKB method. The exact quasinormal frequencies are well approximated by the WKB results.

The matching condition (3.6) leads to a set of discrete quasinormal modes ω_a , labelled by the integer n . In the eikonal regime ($l \gg 1$), the quasinormal modes reduce to

$$\omega_a = l\sqrt{V_{\text{geo}}(x_a)} - i\left(n + \frac{1}{2}\right)\sqrt{-\frac{V_{\text{geo}}^{(2)}(x_a)}{2V_{\text{geo}}(x_a)}}, \quad (3.7)$$

where x_a becomes the global maximum of the geometric potential in the eikonal limit. Using eqs. (2.17) and (2.18), one can express the quasinormal modes (3.7) as

$$\omega_a = \Omega_a l - i\left(n + \frac{1}{2}\right)\lambda_a, \quad (3.8)$$

where Ω_a and λ_a are the angular velocity and the Lyapunov exponent of the unstable circular orbit at the global maximum of the geometric potential, respectively. Interestingly, since the Lyapunov exponent of the unstable circular orbit describes the instability timescale of the geodesic motion, the Lyapunov exponent contributes to the imaginary part of the quasinormal modes. Note that the case with a single maximum of the geometric potential was found to have the same relation between quasinormal modes and circular null geodesics as eq. (3.8) [48]. In table 1, we present the exact and WKB approximated quasinormal frequencies of the lowest-lying modes ($n = 0$) near the global potential maximum for various l in the hairy black hole with $\alpha = 0.9$ and $Q = 1.066$. It shows that the WKB approximation is quite accurate to obtain quasinormal modes trapped at the global maximum of the potential.

3.2 Long-lived modes at minimum

In this subsection, the quasinormal modes of low and high excitations trapped at the minimum of the effective potential are derived via the WKB approximation, respectively. We find that there exist long-lived quasinormal modes, which is related to the stable circular

null geodesic with a purely imaginary Lyapunov exponent. It is noteworthy that the existence of long-lived modes has been reported in the spacetime of ECOs with an unstable photon orbit [42].

We first discuss the low-lying quasinormal modes of frequency ω_{bl} . As illustrated in figure 2, the $(\omega_{bl}^2)^R$ line intersects the effective potential at the turning points x_1, x_2, x_3 and x_4 . Suppose the WKB approximation is valid at a distance δ away from these turning points, where $\delta > 0$ is a small constant. If the $(\omega_{bl}^2)^R$ line is close enough to the local minimum at $x = x_b$, both $x_2 - \delta$ and $x_3 + \delta$ can lie in the interval (x_-, x_+) , in which the effective potential is well approximated by a parabolic expansion. With the approximated parabolic potential, the exact solution of eq. (3.2) can be expressed in terms of parabolic cylinder functions for $x \in (x_-, x_+)$. In addition, the effective potential can be approximated by a linear function near x_1 and x_4 , which leads to the exact solutions in the neighborhoods of x_1 and x_4 . The WKB expansions are required to match the exact solution in $(x_-, x_2 - \delta)$, $(x_3 + \delta, x_+)$ and the neighborhoods of x_1 and x_4 . This matching strategy then gives a family of quasinormal modes [85],

$$\begin{aligned} (\omega_{bl}^2)^R &= V_l(x_b) + \left(n + \frac{1}{2}\right) \sqrt{2V_l^{(2)}(x_b)}, \\ (\omega_{bl}^2)^I &= -\frac{\gamma_n^2}{2 \int_{x_2}^{x_3} \frac{dx}{\sqrt{(\omega_{bl}^R)^2 - V_l(x)}}} \left(e^{-2 \int_{x_1}^{x_2} \sqrt{V_l(x) - (\omega_{bl}^R)^2} dx} + e^{-2 \int_{x_3}^{x_4} \sqrt{V_l(x) - (\omega_{bl}^R)^2} dx} \right), \end{aligned} \quad (3.9)$$

where

$$\gamma_n = \pi^{1/4} \frac{1}{2^{n/2} \sqrt{n!}} \left(\frac{2n+1}{e} \right)^{\frac{1}{2}(n+\frac{1}{2})}. \quad (3.10)$$

Moreover, eq. (3.9) indicates $(\omega_{bl}^2)^R - V_l(x_b) \propto n + \frac{1}{2}$, which means that a large n can drive the $(\omega_{bl}^2)^R$ line away from the local minimum, making $x_2 \in (x_-, x_+)$ and $x_3 \in (x_-, x_+)$ impossible. Therefore, eq. (3.9) is only applicable to the low-lying modes with small n . In figure 3, eqs. (3.9) is used to evaluate the lowest-lying modes ($n = 0$) of the hairy black hole with $\alpha = 0.9$ and $Q = 1.066$, which are denoted by gray dots. Additionally, a direct integration numerically solves eq. (3.2) for exact modes, which are represented by blue dashed lines. We plot the real part ω_{bl}^R against l in the left panel, which shows that the WKB results match well with the numerical ones. As for the imaginary part ω_b^I in the right panel, the WKB results differ a little from the numerical ones for a small l . Nevertheless, the WKB results tend to approach the numerical ones as l increases, which demonstrates that the WKB approximation is accurate enough when l is large enough. To be informative, we provide the WKB approximated values of the long-lived modes of figure 3 and the associated exact values in table 2.

In the large l limit, the real part ω_{bl}^R can be approximated by,

$$\omega_{bl}^R \sim \Omega_b l - i \left(n + \frac{1}{2} \right) \lambda_b \sim \Omega_b l, \quad l \gg 1, \quad (3.11)$$

where Ω_b is the angular velocity of the stable circular orbit at $x = x_b$, and λ_b is the corresponding Lyapunov exponent. Unlike the global maximum case, the Lyapunov exponent

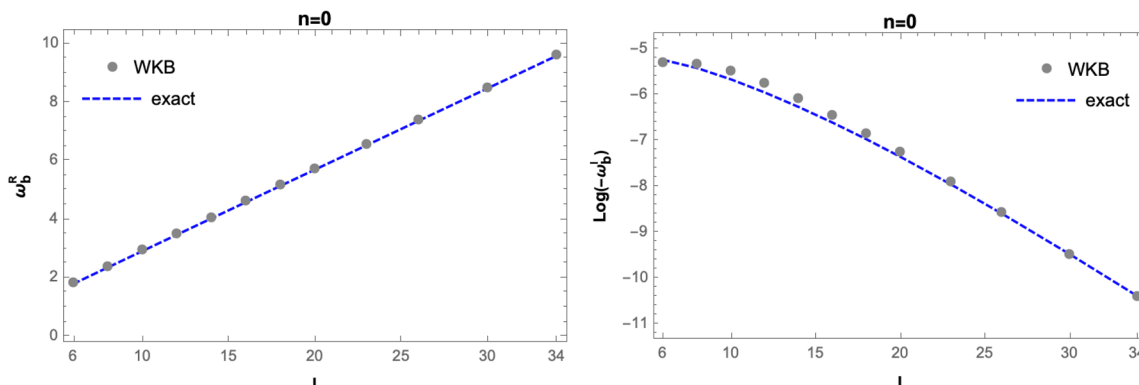


Figure 3. Real (*left*) and imaginary (*right*) parts of the lowest-lying quasinormal modes ($n = 0$) trapped at the stable circular null geodesic. Blue dashed lines represent the exact modes obtained by a numerical method of direct integration, while gray dots denote the WKB results. The real part ω_b^R increases monotonically with l . For a large l , the ratio between ω_b^R and l is the angular velocity of the circular geodesic. The magnitude of ω_b^I decreases exponentially as l increases, which indicates a class of long-lived modes.

	Long-lived Modes at Minimum	
	Exact Modes	WKB Modes
$l = 6$	$\pm 1.8135 - 5.34621 \times 10^{-3}i$	$\pm 1.8154 - 5.00103 \times 10^{-3}i$
$l = 8$	$\pm 2.3749 - 4.47317 \times 10^{-3}i$	$\pm 2.3773 - 4.83434 \times 10^{-3}i$
$l = 10$	$\pm 2.9337 - 3.49474 \times 10^{-3}i$	$\pm 2.9365 - 4.14312 \times 10^{-3}i$
$l = 12$	$\pm 3.4914 - 2.62383 \times 10^{-3}i$	$\pm 3.4943 - 3.16373 \times 10^{-3}i$
$l = 14$	$\pm 4.0484 - 1.91268 \times 10^{-3}i$	$\pm 4.0512 - 2.27558 \times 10^{-3}i$
$l = 16$	$\pm 4.6050 - 1.36019 \times 10^{-3}i$	$\pm 4.6075 - 1.57634 \times 10^{-3}i$
$l = 18$	$\pm 5.1612 - 9.46409 \times 10^{-4}i$	$\pm 5.1635 - 1.06314 \times 10^{-3}i$
$l = 20$	$\pm 5.7171 - 6.45853 \times 10^{-4}i$	$\pm 5.7192 - 7.05101 \times 10^{-4}i$
$l = 23$	$\pm 6.5507 - 3.52859 \times 10^{-4}i$	$\pm 6.5524 - 3.70749 \times 10^{-4}i$
$l = 26$	$\pm 7.3839 - 1.86918 \times 10^{-4}i$	$\pm 7.3854 - 1.90689 \times 10^{-4}i$
$l = 30$	$\pm 8.4944 - 7.72516 \times 10^{-5}i$	$\pm 8.4956 - 7.67052 \times 10^{-5}i$
$l = 34$	$\pm 9.6046 - 3.09851 \times 10^{-5}i$	$\pm 9.6056 - 3.02438 \times 10^{-5}i$

Table 2. WKB approximated and exact values of the long-lived modes in figure 3.

λ_b is purely imaginary for the stable circular null geodesic, and hence contributes to the real part of quasinormal modes. Nevertheless, the correction to ω_{bl}^R due to λ_b is negligible for a small value of n in the large l limit. Hence, the real part of the low-lying quasinormal modes trapped at the stable circular orbit is proportional to the corresponding angular velocity. Schematically in the eikonal limit, the imaginary part ω_{bl}^I can be expressed as

$$\omega_{bl}^I \sim -d \left(e^{-c_1 l} + e^{-c_2 l} \right), \quad l \gg 1, \quad (3.12)$$

where d , c_1 and c_2 are positive constants. It is observed that ω_{bl}^I decays exponentially with respect to l due to the double potential barriers. In fact, ω_{bl}^I is related to the flux density of

leaking modes outside the double potential barriers. An exponentially small value of ω_{bl}^I indicates that the double potential barriers trap these modes in the potential valley with an exponentially large damping time. The quasinormal modes living in the vicinity of the stable null geodesic are thus dubbed as the long-lived modes. Since the long-lived modes can accumulate around the stable null geodesic, their backreaction onto spacetime may render the hairy black holes with a double-peak structure unstable [42–44].

To study quasinormal modes at high excitation ($n \gg 1$), we consider the $(\omega_{bh}^2)^R$ line at some distance away from the local minimum, which is illustrated in figure 2. In the vicinity of each turning point, the effective potential can be approximated by a linear function. Then in the neighborhoods of the turning points, eq. (3.2) can be exactly solved in terms of Airy functions. Away from the turning points, WKB solutions provide a good approximation. To obtain a complete solution, the WKB solutions should be smoothly glued up by the exact solutions near the turning points, which leads to the generalized Born-Sommerfeld quantization rule [85, 86],

$$\int_{x_2}^{x_3} \sqrt{\omega_{bh}^2 - V_l(x)} dx - \frac{i}{4} \left(e^{-2 \int_{x_1}^{x_2} \sqrt{V_l(x) - \omega_{bh}^2} dx} + e^{-2 \int_{x_3}^{x_4} \sqrt{V_l(x) - \omega_{bh}^2} dx} \right) = \pi \left(n + \frac{1}{2} \right). \quad (3.13)$$

In the large l limit, we extract the real part of quasinormal modes from the quantization rule (3.13), which reads

$$\int_{x_2}^{x_3} \sqrt{(\omega_{bh}^R)^2 - V_l(x)} dx = \pi \left(n + \frac{1}{2} \right). \quad (3.14)$$

After the real part ω_{bh}^R is obtained, the imaginary part ω_{bh}^I is then given by

$$\omega_{bh}^I = - \frac{1}{4\omega_{bh}^R \int_{x_2}^{x_3} \frac{\sigma(x)}{\sqrt{(\omega_{bh}^R)^2 - V_l(x)}} dx} \left(e^{-2 \int_{x_1}^{x_2} \sqrt{V_l(x) - (\omega_{bh}^R)^2} dx} + e^{-2 \int_{x_3}^{x_4} \sqrt{V_l(x) - (\omega_{bh}^R)^2} dx} \right), \quad (3.15)$$

where

$$\sigma(x) = 2 \cos^2 \left(-\frac{\pi}{4} + \int_{x_2}^x \sqrt{(\omega_{bh}^R)^2 - V_l(x)} dx \right). \quad (3.16)$$

Since the $(\omega_{bh}^2)^R$ line is not close to the local minimum, the left-hand side of eq. (3.14) becomes large in the eikonal limit, leading to a large n . Thus, eqs. (3.14) and (3.15) describe the quasinormal modes at high excitation with $n \gg 1$. In this case, $\sigma(x)$ oscillates dramatically between x_2 and x_3 , and hence one has $\sigma(x) \approx 1$ under the integration of eq. (3.15). Consequently, the imaginary part of high excitation modes (3.15) can also be schematically written as eq. (3.12) in the eikonal limit. So for $l \gg 1$, the quasinormal modes at high excitation are also long-lived modes.

3.3 Sub-long-lived modes at local maximum

Finally, the quasinormal modes of frequency ω_c , which live near the smaller local maximum (i.e., the local maximum smaller than the global maximum), are investigated. As illustrated in figure 2, we consider the $(\omega_c^2)^R$ line lying in the vicinity of the local maximum at $x = x_c$,

which is associated with the outer unstable circular null geodesic. Following the analogous strategy as before, the effective potential is approximated with a parabola in the interval (x_-, x_+) , and a linear function near the turning points x_1 and x_2 . In addition, the turning points x_3 and x_4 are assumed to lie in (x_-, x_+) , which means that the WKB expansions near x_3 and x_4 can match the exact solution with the parabolic potential. Considering the boundary conditions and matching the WKB expansions with the exact solutions near the turning points, we find the frequency of the quasinormal modes is determined by (see appendix A for the derivation)

$$\int_{x_2}^{x_3} \sqrt{\omega_c^2 - V_l(x)} dx + \xi + \frac{i}{4} e^{-2 \int_{x_1}^{x_2} \sqrt{V_l(x) - \omega_c^2} dx} = \left(n + \frac{1}{4}\right) \pi, \quad (3.17)$$

where ξ is defined by

$$e^{-2i\xi} = e^{-i\pi\nu + (\nu + 1/2)} \left(\nu + \frac{1}{2}\right)^{-(\nu + \frac{1}{2})} \frac{\sqrt{2\pi}}{\Gamma(-\nu)}, \nu + \frac{1}{2} = i \frac{\omega_c^2 - V_l(x_c)}{\sqrt{-2V_l^{(2)}(x_c)}}. \quad (3.18)$$

Roughly speaking, the trapping in the potential valley and the tunneling through the left potential barrier result in the first and last terms of eq. (3.17), respectively.

Since the distance between x_3 and x_4 is assumed to be small, the value of $\nu + 1/2$ should be tiny compared to l . In fact, the matching condition (3.17) is valid to evaluate quasinormal modes when the condition $|\nu + 1/2| \ll l$ is satisfied [85]. Note that the valley of the effective potential becomes deeper/shallower as l increases/decreases. For a given n , a large l would drive the $(\omega_c^2)^R$ line away from the local maximum at $x = x_c$, thus making the first term in the left-hand side of eq. (3.17) small enough to satisfy eq. (3.17). However, if $(\omega_c^2)^R$ is not close enough to the local maximum, the condition $|\nu + 1/2| \ll l$ can be violated, which indicates that the WKB result (3.17) is not a good approximation when l is too large. In the case with large l , the effective potential can be approximated by a linear function near the turning points x_3 and x_4 , which leads to the WKB results (3.14) and (3.15). For an even larger l , the $(\omega_c^2)^R$ line can lie close to the minimum of the potential, which corresponds to the aforementioned long-lived modes at low excitations. On the other hand, when l decreases, the first term in the left-hand side of eq. (3.17) requires that the $(\omega_c^2)^R$ line moves toward the local maximum when n is fixed. Interestingly, a too small l can make $(\omega_c^2)^R$ greater than the local maximum, hence rendering the turning points x_3 and x_4 unable to exist. So the WKB result (3.17) may cease to exist when l is too small.

In figure 4, two branches of quasinormal modes are obtained using eqs. (3.17) and (3.18), i.e., $n = 0$ in the upper row and $n = 1$ in the lower row. Moreover, we also plot the value of $|\nu + 1/2|/l$ as a function of l for each branch of the quasinormal modes in the right column, which checks the validity of the WKB approximation. Compared with exact modes (blue dashed lines), the real part of the quasinormal modes (gray dots) is well approximated by the WKB method. By contrast, the imaginary part of the WKB result matches that of exact modes well except when l is too large, for which, as displayed in the right column, the condition $|\nu + 1/2| \ll l$ is not well satisfied. It also shows that there exists a lowest l for each branch (e.g., $l = 6$ for $n = 0$ and $l = 32$ for $n = 1$), below which the WKB results do

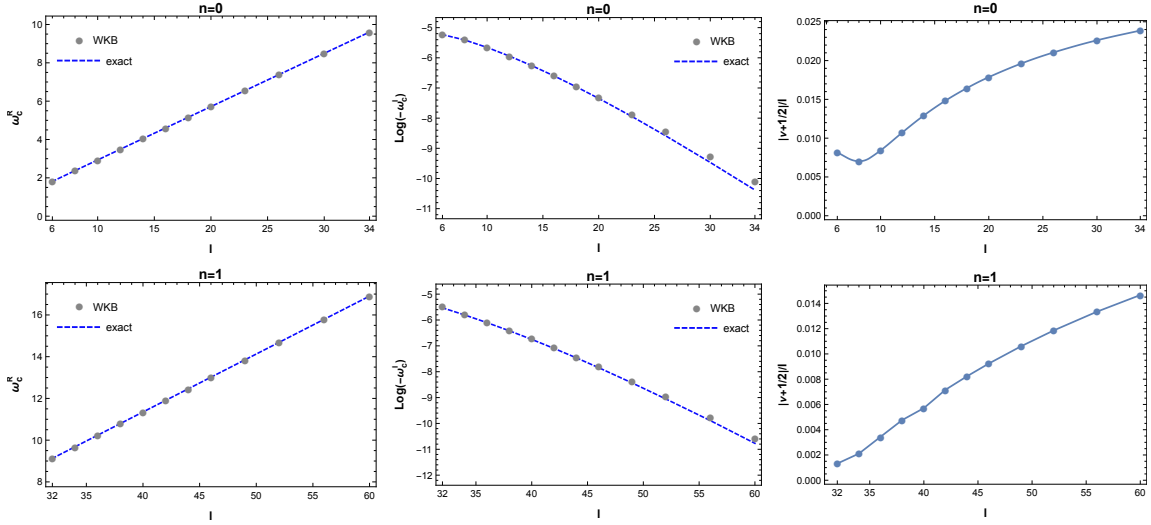


Figure 4. Real part (*left*), imaginary part (*middle*) and $|\nu + 1/2|/l$ (*right*) of the quasinormal modes, which are trapped at the local maximum of the effective potential, for the branches of $n = 0$ (*upper*) and $n = 1$ (*lower*). The left column shows that the real parts of the WKB results (gray dots) agree well with these of exact modes (blue dashed lines). In the middle column, the imaginary parts of WKB and exact results match well for small l , and start to deviate from each other when l becomes larger. As shown in the right column, the value of $|\nu + 1/2|/l$ grows as l increases, which means that the WKB approximation may not be accurate for a large l .

not exist. Note that the exact modes of $n = 0$ presented in figures 3 and 4 are precisely the same. As expected, the exact modes are accurately described by the WKB results (3.17) and (3.9) for small and large l , respectively.

To find the relation between the quasinormal modes and the parameters of circular null geodesics, we focus on the limit $|\nu + 1/2| \ll 1$. In this limit, the matching condition (3.17) is further simplified (see appendix A for the derivation),

$$\begin{aligned}
 (\omega_c^2)^R &\approx V_l(x_c) + \frac{\sqrt{-2V_l^{(2)}(x_c)}2\pi I}{I^2 + \pi^2/4} \left(n - n^* - \frac{e^{-2\int_{x_1}^{x_2} \sqrt{V_l(x) - \omega_c^2} dx}}{8I} \right), \\
 (\omega_c^2)^I &\approx -\frac{\log 2}{2I} \sqrt{-2V_l^{(2)}(x_c)} - \frac{\sqrt{-2V_l^{(2)}(x_c)}\pi^2}{I^2 + \pi^2/4} \left(n - n^* - \frac{I e^{-2\int_{x_1}^{x_2} \sqrt{V_l(x) - \omega_c^2} dx}}{2\pi^2} \right), \quad (3.19)
 \end{aligned}$$

where I is

$$\begin{aligned}
 I &= \log \left(\sqrt{-2V_l^{(2)}(x_c)} (x_c - x_2)^2 \right) \\
 &\quad + 2 \int_{x_2}^{x_c} \left(\frac{\sqrt{-2V_l^{(2)}(x_c)}}{2\sqrt{V_l(x_c) - V_l(x)}} - \frac{1}{(x_c - x)} \right) dx + (\gamma + \log 2\pi), \quad (3.20)
 \end{aligned}$$

with a constant $\gamma = 0.5772$. Here, the number n^* is defined as

$$n^* \equiv \frac{1}{\pi} \int_{x_2}^{x_c} \sqrt{V_l(x_c) - V_l(x)} dx + \frac{\log 2}{8I} - \frac{1}{2}, \quad (3.21)$$

		Exact Modes	WKB Modes	$2\pi(n - n^*)/I$
$n = 0$	$l = 5$	$\pm 1.5308 - 0.00556i$	$\pm 1.5323 - 0.00479i$	0.0006
	$l = 6$	$\pm 1.8135 - 0.00535i$	$\pm 1.8148 - 0.00463i$	-0.0010
$n = 1$	$l = 31$	$\pm 8.8483 - 0.00453i$	$\pm 8.8486 - 0.00421i$	0.0257
	$l = 32$	$\pm 9.1263 - 0.00397i$	$\pm 9.1267 - 0.00372i$	-0.0033
$n = 2$	$l = 54$	$\pm 15.3090 - 0.00402i$	$\pm 15.3092 - 0.00381i$	0.0145
	$l = 55$	$\pm 15.5871 - 0.00353i$	$\pm 15.5874 - 0.00336i$	-0.0135
$n = 3$	$l = 76$	$\pm 21.4905 - 0.00406i$	$\pm 21.4906 - 0.00385i$	0.0256
	$l = 77$	$\pm 21.7686 - 0.00359i$	$\pm 21.7688 - 0.00343i$	-0.0016
$n = 4$	$l = 99$	$\pm 27.9497 - 0.00365i$	$\pm 27.9498 - 0.00349i$	0.0080
	$l = 100$	$\pm 28.2278 - 0.00323i$	$\pm 28.2281 - 0.00309i$	-0.0186
$n = 5$	$l = 121$	$\pm 34.1306 - 0.00371i$	$\pm 34.1307 - 0.00355i$	0.0165
	$l = 122$	$\pm 34.4088 - 0.00330i$	$\pm 34.4089 - 0.00317i$	-0.0096

Table 3. Pairs of sub-long-lived modes for different values of n . These quasinormal modes are evaluated near the local maximum of the effective potential, corresponding to an unstable circular null geodesic. The exact modes are numerically obtained using a direct integration, which can be approximated well by the WKB method for small magnitude of $2\pi(n - n^*)/I$.

which can be interpreted as the number of a resonance filling the potential well until $(\omega_c^2)^R = V_l(x_c)$ in the eikonal limit. Moreover, the condition $|\nu + 1/2| \ll 1$ requires

$$\frac{2\pi|n - n^*|}{I} \ll 1, \tag{3.22}$$

which provides a constraint on n and l . For quasinormal modes of given n , there appears to exist a pair of adjacent integers l that well satisfy the constraint (3.22). For $n \leq 5$, table 3 displays the quasinormal modes with such adjacent l . In this case, it shows that the exact (obtained by a numerical direct integration method) and WKB (obtained from eq. (3.19)) results agree well with each other.

When n is large enough, the value of l satisfying the constraint (3.22) can be arbitrarily large. In the large l limit, eq. (3.19) reduces to

$$\begin{aligned} \omega_c^R &\sim l\sqrt{V_{\text{geo}}(x_c)} = \Omega_c l, \\ \omega_c^I &\sim -\frac{\log 2}{2\log l}\lambda_c, \end{aligned} \tag{3.23}$$

where we use $I \sim \log l$ for $l \gg 1$. Here Ω_c is the angular velocity of the unstable circular null geodesic at $x = x_c$, and λ_c is the corresponding Lyapunov exponent. For these quasinormal modes, the turning points x_3 and x_4 are very close to x_c , and hence their real part ω_c^R is proportional to the angular velocity Ω_c . Similar to the global maximum case, the Lyapunov exponent of the outer unstable circular orbit contributes to the imaginary part of the quasinormal modes. However, these quasinormal modes can temporarily trap in the potential valley, which gives a logarithmically decaying factor $1/\log l$ in their imaginary part. For this reason, this type of quasinormal modes is dubbed as sub-long-lived modes.

4 Conclusions

In this paper, we studied quasinormal modes of a scalar field in hairy black hole spacetime, where the scalar field is minimally coupled to the gravity sector and non-minimally coupled to the electromagnetic field with an exponential coupling function. Intriguingly, the hairy black holes have been demonstrated to possess two unstable and one stable circular null geodesics on the equatorial plane outside the event horizon, corresponding to two maxima and one minimum of the geometric potential for null geodesic motion, respectively. It showed that, apart from a constant prefactor, the effective potential governing quasinormal modes of the scalar perturbation can be well approximated by the geometric potential in the eikonal regime. To explore the relation between quasinormal modes and the parameters of the circular null geodesics, we used the WKB method to compute quasinormal modes living near the global maximum, the smaller local maximum and the minimum of the effective potential.

In the large l limit, the real part of these quasinormal modes was shown to be proportional to the angular velocity of the corresponding circular null geodesics, which implies that the quasinormal modes can be related to particles traveling along the circular null geodesics. However, since the imaginary part ω_I describes the perturbation decay timescale, ω_I was found to have distinct behaviors, depending on the location of the quasinormal modes. For the quasinormal modes near the global maximum, ω_I can be interpreted as slowly leaking out of particles trapped at the unstable circular null geodesics, and is related to the Lyapunov exponent, which reflects the instability timescale of geodesic motion. On the other hand, the effective potential valley between two maxima plays a key role in determining the behavior of ω_I of quasinormal modes near the local maximum and the minimum in the eikonal regime. When $l \gg 1$, the depth of the potential valley was found to be proportional to l^2 . The quasinormal modes living at the bottom of the potential valley (i.e., the minimum) are metastable states with tunneling out through the high potential barriers, which gives that ω_I decays exponentially with respect to l . There appeared to be two contributions to ω_I of the quasinormal modes near the local maximum, i.e., classical leaking out from the unstable circular null geodesics, which makes ω_I proportional to the Lyapunov exponent, and tunneling out through the global maximum barrier, which makes ω_I inversely proportional to $\log l$. Due to the exponential and logarithmic suppressions in ω_I , the quasinormal modes in the neighborhoods of the minimum and local maximum can live for a long time, and hence were dubbed as long-lived and sub-long-lived modes, respectively.

In this paper, we focused on quasinormal modes near potential extrema. One may wonder whether there exist some quasinormal modes, which live between the extrema and are not exactly associated with any of them. We exhibit the $l = 5$ quasinormal modes of the hairy black hole with $\alpha = 0.76$ and $Q = 1.045$ in figure 5, where horizontal lines denote the real parts of the exact numerical quasinormal modes ω^2 . The quasinormal modes at the global maximum, the smaller maximum and the minimum of the potential are represented by red, blue and green lines, respectively. Moreover, the exact numerical and the WKB approximated quasinormal frequencies of the modes are presented in the right frame, which shows that they are in good agreement. Interestingly, between the quasinormal modes at the

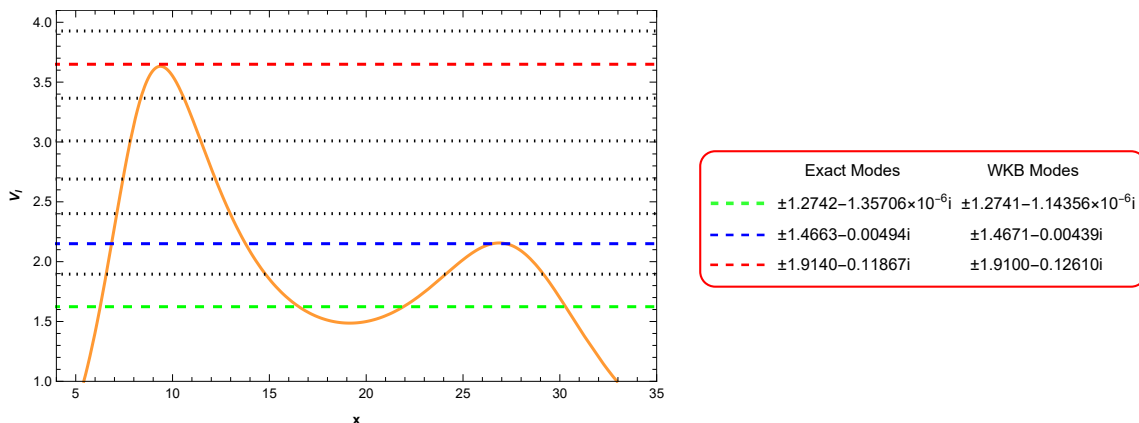


Figure 5. The $l = 5$ quasinormal modes of the hairy black hole with $\alpha = 0.76$ and $Q = 1.045$. The orange line denotes the double-peak effective potential against the tortoise coordinate x , and the horizontal lines represent the real parts of exact quasinormal modes ω^2 . Apart from the quasinormal modes near the global maximum (red line), the smaller maximum (blue line) and the minimum (green line) of the potential, there exist quasinormal modes (black dotted lines) between the potential extrema, which can not be determined accurately by the WKB approximation.

potential extrema, there indeed appear several quasinormal modes, which are displayed as black dotted lines. We find that the exact quasinormal frequencies of these modes noticeably deviate from the WKB results, indicating that these quasinormal modes do not relate to any extremum of the potential. As l increases, the potential peaks become higher, and the potential valley becomes deeper, which, similar to energy levels in a finite square potential, introduces more quasinormal modes living near and between the potential extrema. In particular, it is expected that, when $l \gg 1$, a family of quasinormal modes is trapped at each potential extremum, meaning that three extremum of double-peak potentials lead to three families of quasinormal modes near the potential extrema.

The long-lived modes may accumulate along the stable circular orbit, and eventually develop a non-linear instability. Moreover for a spinning object, the existence of long-lived modes may also trigger an ergoregion instability at the linear level in the static limit [42]. These instabilities imply that long-lived modes trapped at the stable circular orbit could destabilize the background spacetime by their backreaction. In the future studies, it is of great interest to further address the instabilities of long-lived and sub-long-lived modes in a hairy black hole, and explore the end point of a hairy black hole possessing three circular null geodesics in a dynamic evolution.

Acknowledgments

We are grateful to Yiqian Chen and Qingyu Gan for useful discussions and valuable comments. This work is supported in part by NSFC (Grant No. 12105191, 11947225 and 11875196). Houwen Wu is supported by the International Visiting Program for Excellent Young Scholars of Sichuan University.

A Derivations of eqs. (3.17) and (3.19)

In this appendix, we follow [84–86] to give derivations of eqs. (3.17) and (3.19). As presented in figure 2, we consider the $(\omega_c^2)^R$ line close to the local maximum at $x = x_c$, and discuss the WKB solutions in different ranges of x . When $x_2 < x < x_3$, the WKB solution is

$$\Psi_{\text{I}}(x) \sim \left[\omega_c^2 - V_l(x)\right]^{-1/4} \sin\left(\int_{x_2}^x \sqrt{\omega_c^2 - V_l(x')} dx' + \frac{\pi}{4} + \frac{i}{4} e^{-2\int_{x_1}^{x_2} \sqrt{V_l(x) - \omega_c^2} dx}\right). \quad (\text{A.1})$$

For $x > x_4$, the outgoing WKB solution is

$$\Psi_{\text{III}}(x) \sim \left[\omega_c^2 - V_l(x)\right]^{-1/4} e^{i\int_{x_4}^x \sqrt{\omega_c^2 - V_l(x')} dx'}. \quad (\text{A.2})$$

In the interval (x_-, x_+) , the effective potential is approximated by a parabolic expansion, for which the perturbative equation (3.2) can be exactly solved. To match the WKB solution (A.2) in the region (x_4, x_+) , the exact solution $\Psi_{\text{II}}(x)$ is then given by

$$\Psi_{\text{II}}(x) \sim D_\nu(t), \quad (\text{A.3})$$

where $D_\nu(t)$ represents the parabolic cylinder function, ν is defined in eq. (3.18), and $t \equiv e^{i\pi/4}[-2V_l^{(2)}(x_c)]^{1/4}(x - x_c)$. On the other hand, to match the solution (A.3) with the exact solution $\Psi_{\text{II}}(x)$ in the region (x_-, x_3) , the WKB solution for $x_2 < x < x_3$ should be

$$\Psi_{\text{I}}'(x) \sim \left[\omega_c^2 - V_l(x)\right]^{-1/4} \sin\left(\int_x^{x_3} \sqrt{\omega_c^2 - V_l(x')} dx' + \xi + \frac{\pi}{2}\right), \quad (\text{A.4})$$

where ξ is defined in eq. (3.18). To satisfy $\Psi_{\text{I}}(x) \propto \Psi_{\text{I}}'(x)$ for $x \in (x_2, x_3)$, the sum of the components of sine functions in eqs. (A.1) and (A.4) must be a multiple of π , which gives eq. (3.17).

In the limit $|\nu + 1/2| \ll 1$, the first term of the left-hand side of eq. (3.17) becomes

$$\begin{aligned} \int_{x_2}^{x_3} \sqrt{\omega_c^2 - V_l(x)} dx &= \int_{x_2}^{x_-} \sqrt{\omega_c^2 - V_l(x)} dx + \int_{x_-}^{x_3} \sqrt{\omega_c^2 - V_l(x)} dx \\ &\approx \int_{x_2}^{x_c} \sqrt{V_l(x_c) - V_l(x)} dx \\ &\quad + \frac{ia}{2} \left(\log(ia) - 1 - \log\left[\sqrt{-2V_l^{(2)}(x_c)}(x_c - x_2)\right]^2 \right) \\ &\quad - ia \int_{x_2}^{x_c} \left(\frac{\sqrt{-2V_l^{(2)}(x_c)}}{2\sqrt{V_l(x_c) - V_l(x)}} - \frac{1}{(x_c - x)} \right) dx, \end{aligned} \quad (\text{A.5})$$

where we replace the effective potential by a parabola in the region (x_-, x_c) , and $a = \nu + 1/2$. Moreover, ξ in eq. (3.17) can be expanded as

$$\xi \approx \frac{i}{2} \left(-i\pi a - a \ln a + \frac{\ln 2}{2} + \frac{i\pi}{2} + a[1 - (\gamma + \ln 2 + \ln \pi)] \right), \quad (\text{A.6})$$

where $\gamma = 0.5772$. From eqs. (3.17), (A.5) and (A.6), one can extract the real and imaginary parts of ω_c^2 , which gives eq. (3.19).

Open Access. This article is distributed under the terms of the Creative Commons Attribution License ([CC-BY 4.0](https://creativecommons.org/licenses/by/4.0/)), which permits any use, distribution and reproduction in any medium, provided the original author(s) and source are credited.

References

- [1] LIGO SCIENTIFIC and VIRGO collaborations, *Observation of Gravitational Waves from a Binary Black Hole Merger*, *Phys. Rev. Lett.* **116** (2016) 061102 [[arXiv:1602.03837](https://arxiv.org/abs/1602.03837)] [[INSPIRE](#)].
- [2] EVENT HORIZON TELESCOPE collaboration, *First M87 Event Horizon Telescope Results. I. The Shadow of the Supermassive Black Hole*, *Astrophys. J. Lett.* **875** (2019) L1 [[arXiv:1906.11238](https://arxiv.org/abs/1906.11238)] [[INSPIRE](#)].
- [3] EVENT HORIZON TELESCOPE collaboration, *First M87 Event Horizon Telescope Results. II. Array and Instrumentation*, *Astrophys. J. Lett.* **875** (2019) L2 [[arXiv:1906.11239](https://arxiv.org/abs/1906.11239)] [[INSPIRE](#)].
- [4] EVENT HORIZON TELESCOPE collaboration, *First M87 Event Horizon Telescope Results. III. Data Processing and Calibration*, *Astrophys. J. Lett.* **875** (2019) L3 [[arXiv:1906.11240](https://arxiv.org/abs/1906.11240)] [[INSPIRE](#)].
- [5] EVENT HORIZON TELESCOPE collaboration, *First M87 Event Horizon Telescope Results. IV. Imaging the Central Supermassive Black Hole*, *Astrophys. J. Lett.* **875** (2019) L4 [[arXiv:1906.11241](https://arxiv.org/abs/1906.11241)] [[INSPIRE](#)].
- [6] EVENT HORIZON TELESCOPE collaboration, *First M87 Event Horizon Telescope Results. V. Physical Origin of the Asymmetric Ring*, *Astrophys. J. Lett.* **875** (2019) L5 [[arXiv:1906.11242](https://arxiv.org/abs/1906.11242)] [[INSPIRE](#)].
- [7] EVENT HORIZON TELESCOPE collaboration, *First M87 Event Horizon Telescope Results. VI. The Shadow and Mass of the Central Black Hole*, *Astrophys. J. Lett.* **875** (2019) L6 [[arXiv:1906.11243](https://arxiv.org/abs/1906.11243)] [[INSPIRE](#)].
- [8] E. Berti, V. Cardoso, J.A. Gonzalez and U. Sperhake, *Mining information from binary black hole mergers: A comparison of estimation methods for complex exponentials in noise*, *Phys. Rev. D* **75** (2007) 124017 [[gr-qc/0701086](https://arxiv.org/abs/gr-qc/0701086)] [[INSPIRE](#)].
- [9] V. Ferrari and B. Mashhoon, *New approach to the quasinormal modes of a black hole*, *Phys. Rev. D* **30** (1984) 295 [[INSPIRE](#)].
- [10] H.-P. Nollert, *TOPICAL REVIEW: Quasinormal modes: the characteristic ‘sound’ of black holes and neutron stars*, *Class. Quant. Grav.* **16** (1999) R159 [[INSPIRE](#)].
- [11] G.T. Horowitz and V.E. Hubeny, *Quasinormal modes of AdS black holes and the approach to thermal equilibrium*, *Phys. Rev. D* **62** (2000) 024027 [[hep-th/9909056](https://arxiv.org/abs/hep-th/9909056)] [[INSPIRE](#)].
- [12] E. Berti and K.D. Kokkotas, *Quasinormal modes of Reissner-Nordström-anti-de Sitter black holes: Scalar, electromagnetic and gravitational perturbations*, *Phys. Rev. D* **67** (2003) 064020 [[gr-qc/0301052](https://arxiv.org/abs/gr-qc/0301052)] [[INSPIRE](#)].
- [13] Y.S. Myung, Y.-W. Kim and Y.-J. Park, *Quasinormal modes from potentials surrounding the charged dilaton black hole*, *Eur. Phys. J. C* **58** (2008) 617 [[arXiv:0809.1933](https://arxiv.org/abs/0809.1933)] [[INSPIRE](#)].
- [14] E. Berti, V. Cardoso and A.O. Starinets, *Quasinormal modes of black holes and black branes*, *Class. Quant. Grav.* **26** (2009) 163001 [[arXiv:0905.2975](https://arxiv.org/abs/0905.2975)] [[INSPIRE](#)].
- [15] R.A. Konoplya and A. Zhidenko, *Quasinormal modes of black holes: From astrophysics to string theory*, *Rev. Mod. Phys.* **83** (2011) 793 [[arXiv:1102.4014](https://arxiv.org/abs/1102.4014)] [[INSPIRE](#)].

- [16] H. Yang, D.A. Nichols, F. Zhang, A. Zimmerman, Z. Zhang and Y. Chen, *Quasinormal-mode spectrum of Kerr black holes and its geometric interpretation*, *Phys. Rev. D* **86** (2012) 104006 [[arXiv:1207.4253](#)] [[INSPIRE](#)].
- [17] G.B. Cook and M. Zalutskiy, *Purely imaginary quasinormal modes of the Kerr geometry*, *Class. Quant. Grav.* **33** (2016) 245008 [[arXiv:1603.09710](#)] [[INSPIRE](#)].
- [18] Y.S. Myung and D.-C. Zou, *Quasinormal modes of scalarized black holes in the Einstein-Maxwell-Scalar theory*, *Phys. Lett. B* **790** (2019) 400 [[arXiv:1812.03604](#)] [[INSPIRE](#)].
- [19] R.A. Konoplya, A. Zhidenko and A.F. Zinhailo, *Higher order WKB formula for quasinormal modes and grey-body factors: recipes for quick and accurate calculations*, *Class. Quant. Grav.* **36** (2019) 155002 [[arXiv:1904.10333](#)] [[INSPIRE](#)].
- [20] J. Luis Blázquez-Salcedo, C.A.R. Herdeiro, S. Kahlen, J. Kunz, A.M. Pombo and E. Radu, *Quasinormal modes of hot, cold and bald Einstein-Maxwell-scalar black holes*, *Eur. Phys. J. C* **81** (2021) 155 [[arXiv:2008.11744](#)] [[INSPIRE](#)].
- [21] D.D. Doneva, S.S. Yazadjiev, K.D. Kokkotas and I.Z. Stefanov, *Quasi-normal modes, bifurcations and non-uniqueness of charged scalar-tensor black holes*, *Phys. Rev. D* **82** (2010) 064030 [[arXiv:1007.1767](#)] [[INSPIRE](#)].
- [22] J.L. Blázquez-Salcedo, D.D. Doneva, J. Kunz and S.S. Yazadjiev, *Radial perturbations of the scalarized Einstein-Gauss-Bonnet black holes*, *Phys. Rev. D* **98** (2018) 084011 [[arXiv:1805.05755](#)] [[INSPIRE](#)].
- [23] Y.S. Myung and D.-C. Zou, *Instability of Reissner-Nordström black hole in Einstein-Maxwell-scalar theory*, *Eur. Phys. J. C* **79** (2019) 273 [[arXiv:1808.02609](#)] [[INSPIRE](#)].
- [24] Y.S. Myung and D.-C. Zou, *Stability of scalarized charged black holes in the Einstein-Maxwell-Scalar theory*, *Eur. Phys. J. C* **79** (2019) 641 [[arXiv:1904.09864](#)] [[INSPIRE](#)].
- [25] D.-C. Zou and Y.S. Myung, *Radial perturbations of the scalarized black holes in Einstein-Maxwell-conformally coupled scalar theory*, *Phys. Rev. D* **102** (2020) 064011 [[arXiv:2005.06677](#)] [[INSPIRE](#)].
- [26] G. Guo, P. Wang, H. Wu and H. Yang, *Scalarized Einstein-Maxwell-scalar black holes in anti-de Sitter spacetime*, *Eur. Phys. J. C* **81** (2021) 864 [[arXiv:2102.04015](#)] [[INSPIRE](#)].
- [27] V. Cardoso, J.L. Costa, K. Destounis, P. Hintz and A. Jansen, *Quasinormal modes and Strong Cosmic Censorship*, *Phys. Rev. Lett.* **120** (2018) 031103 [[arXiv:1711.10502](#)] [[INSPIRE](#)].
- [28] Q. Gan, G. Guo, P. Wang and H. Wu, *Strong cosmic censorship for a scalar field in a Born-Infeld-de Sitter black hole*, *Phys. Rev. D* **100** (2019) 124009 [[arXiv:1907.04466](#)] [[INSPIRE](#)].
- [29] Q. Gan, P. Wang, H. Wu and H. Yang, *Strong Cosmic Censorship for a Scalar Field in an Einstein-Maxwell-Gauss-Bonnet-de Sitter Black Hole*, *Chin. Phys. C* **45** (2021) 025103 [[arXiv:1911.10996](#)] [[INSPIRE](#)].
- [30] J.P.S. Lemos and O.B. Zaslavskii, *Black hole mimickers: Regular versus singular behavior*, *Phys. Rev. D* **78** (2008) 024040 [[arXiv:0806.0845](#)] [[INSPIRE](#)].
- [31] P.V.P. Cunha, J.A. Font, C. Herdeiro, E. Radu, N. Sanchis-Gual and M. Zilhão, *Lensing and dynamics of ultracompact bosonic stars*, *Phys. Rev. D* **96** (2017) 104040 [[arXiv:1709.06118](#)] [[INSPIRE](#)].
- [32] P.V.P. Cunha and C.A.R. Herdeiro, *Shadows and strong gravitational lensing: a brief review*, *Gen. Rel. Grav.* **50** (2018) 42 [[arXiv:1801.00860](#)] [[INSPIRE](#)].

- [33] R. Shaikh, P. Banerjee, S. Paul and T. Sarkar, *A novel gravitational lensing feature by wormholes*, *Phys. Lett. B* **789** (2019) 270 [Erratum *ibid.* **791** (2019) 422] [[arXiv:1811.08245](#)] [[INSPIRE](#)].
- [34] H. Huang and J. Yang, *Charged Ellis Wormhole and Black Bounce*, *Phys. Rev. D* **100** (2019) 124063 [[arXiv:1909.04603](#)] [[INSPIRE](#)].
- [35] M. Wielgus, J. Horak, F. Vincent and M. Abramowicz, *Reflection-asymmetric wormholes and their double shadows*, *Phys. Rev. D* **102** (2020) 084044 [[arXiv:2008.10130](#)] [[INSPIRE](#)].
- [36] J. Yang and H. Huang, *Trapping horizons of the evolving charged wormhole and black bounce*, *Phys. Rev. D* **104** (2021) 084005 [[arXiv:2104.11134](#)] [[INSPIRE](#)].
- [37] J. Peng, M. Guo and X.-H. Feng, *Observational signature and additional photon rings of an asymmetric thin-shell wormhole*, *Phys. Rev. D* **104** (2021) 124010 [[arXiv:2102.05488](#)] [[INSPIRE](#)].
- [38] Z. Mark, A. Zimmerman, S.M. Du and Y. Chen, *A recipe for echoes from exotic compact objects*, *Phys. Rev. D* **96** (2017) 084002 [[arXiv:1706.06155](#)] [[INSPIRE](#)].
- [39] P. Bueno, P.A. Cano, F. Goelen, T. Hertog and B. Vercknocke, *Echoes of Kerr-like wormholes*, *Phys. Rev. D* **97** (2018) 024040 [[arXiv:1711.00391](#)] [[INSPIRE](#)].
- [40] V. Cardoso and P. Pani, *Testing the nature of dark compact objects: a status report*, *Living Rev. Rel.* **22** (2019) 4 [[arXiv:1904.05363](#)] [[INSPIRE](#)].
- [41] M.-Y. Ou, M.-Y. Lai and H. Huang, *Echoes from asymmetric wormholes and black bounce*, *Eur. Phys. J. C* **82** (2022) 452 [[arXiv:2111.13890](#)] [[INSPIRE](#)].
- [42] V. Cardoso, L.C.B. Crispino, C.F.B. Macedo, H. Okawa and P. Pani, *Light rings as observational evidence for event horizons: long-lived modes, ergoregions and nonlinear instabilities of ultracompact objects*, *Phys. Rev. D* **90** (2014) 044069 [[arXiv:1406.5510](#)] [[INSPIRE](#)].
- [43] J. Keir, *Slowly decaying waves on spherically symmetric spacetimes and ultracompact neutron stars*, *Class. Quant. Grav.* **33** (2016) 135009 [[arXiv:1404.7036](#)] [[INSPIRE](#)].
- [44] M. Guo, Z. Zhong, J. Wang and S. Gao, *Light rings and long-lived modes in quasiblack hole spacetimes*, *Phys. Rev. D* **105** (2022) 024049 [[arXiv:2108.08967](#)] [[INSPIRE](#)].
- [45] J.L. Friedman, *Ergosphere instability*, *Commun. Math. Phys.* **63** (1978) 243.
- [46] C.B.M.H. Chirenti and L. Rezzolla, *On the ergoregion instability in rotating gravastars*, *Phys. Rev. D* **78** (2008) 084011 [[arXiv:0808.4080](#)] [[INSPIRE](#)].
- [47] P. Pani, V. Cardoso, M. Cadoni and M. Cavaglia, *Ergoregion instability of black hole mimickers*, *PoS BHGRS* (2008) 027 [[arXiv:0901.0850](#)] [[INSPIRE](#)].
- [48] V. Cardoso, A.S. Miranda, E. Berti, H. Witek and V.T. Zanchin, *Geodesic stability, Lyapunov exponents and quasinormal modes*, *Phys. Rev. D* **79** (2009) 064016 [[arXiv:0812.1806](#)] [[INSPIRE](#)].
- [49] R.A. Konoplya and Z. Stuchlík, *Are eikonal quasinormal modes linked to the unstable circular null geodesics?*, *Phys. Lett. B* **771** (2017) 597 [[arXiv:1705.05928](#)] [[INSPIRE](#)].
- [50] K. Jusufi, *Quasinormal Modes of Black Holes Surrounded by Dark Matter and Their Connection with the Shadow Radius*, *Phys. Rev. D* **101** (2020) 084055 [[arXiv:1912.13320](#)] [[INSPIRE](#)].

- [51] B. Cuadros-Melgar, R.D.B. Fontana and J. de Oliveira, *Analytical correspondence between shadow radius and black hole quasinormal frequencies*, *Phys. Lett. B* **811** (2020) 135966 [[arXiv:2005.09761](#)] [[INSPIRE](#)].
- [52] W.-L. Qian, K. Lin, X.-M. Kuang, B. Wang and R.-H. Yue, *Quasinormal modes in two-photon autocorrelation and the geometric-optics approximation*, *Eur. Phys. J. C* **82** (2022) 188 [[arXiv:2109.02844](#)] [[INSPIRE](#)].
- [53] W. Israel, *Event horizons in static vacuum space-times*, *Phys. Rev.* **164** (1967) 1776 [[INSPIRE](#)].
- [54] B. Carter, *Axisymmetric Black Hole Has Only Two Degrees of Freedom*, *Phys. Rev. Lett.* **26** (1971) 331 [[INSPIRE](#)].
- [55] R. Ruffini and J.A. Wheeler, *Introducing the black hole*, *Phys. Today* **24** (1971) 30 [[INSPIRE](#)].
- [56] M.S. Volkov and D.V. Galtsov, *NonAbelian Einstein Yang-Mills black holes*, *JETP Lett.* **50** (1989) 346 [[INSPIRE](#)].
- [57] P. Bizon, *Colored black holes*, *Phys. Rev. Lett.* **64** (1990) 2844 [[INSPIRE](#)].
- [58] B.R. Greene, S.D. Mathur and C.M. O'Neill, *Eluding the no hair conjecture: Black holes in spontaneously broken gauge theories*, *Phys. Rev. D* **47** (1993) 2242 [[hep-th/9211007](#)] [[INSPIRE](#)].
- [59] H. Lübeck and I. Moss, *Black holes have skyrmion hair*, *Phys. Lett. B* **176** (1986) 341 [[INSPIRE](#)].
- [60] S. Droz, M. Heusler and N. Straumann, *New black hole solutions with hair*, *Phys. Lett. B* **268** (1991) 371 [[INSPIRE](#)].
- [61] P. Kanti, N.E. Mavromatos, J. Rizos, K. Tamvakis and E. Winstanley, *Dilatonic black holes in higher curvature string gravity*, *Phys. Rev. D* **54** (1996) 5049 [[hep-th/9511071](#)] [[INSPIRE](#)].
- [62] S. Mahapatra, S. Priyadarshinee, G.N. Reddy and B. Shukla, *Exact topological charged hairy black holes in AdS Space in D-dimensions*, *Phys. Rev. D* **102** (2020) 024042 [[arXiv:2004.00921](#)] [[INSPIRE](#)].
- [63] C.A.R. Herdeiro, E. Radu, N. Sanchis-Gual and J.A. Font, *Spontaneous Scalarization of Charged Black Holes*, *Phys. Rev. Lett.* **121** (2018) 101102 [[arXiv:1806.05190](#)] [[INSPIRE](#)].
- [64] D. Astefanesei, C. Herdeiro, A. Pombo and E. Radu, *Einstein-Maxwell-scalar black holes: classes of solutions, dyons and extremality*, *JHEP* **10** (2019) 078 [[arXiv:1905.08304](#)] [[INSPIRE](#)].
- [65] P.G.S. Fernandes, C.A.R. Herdeiro, A.M. Pombo, E. Radu and N. Sanchis-Gual, *Charged black holes with axionic-type couplings: Classes of solutions and dynamical scalarization*, *Phys. Rev. D* **100** (2019) 084045 [[arXiv:1908.00037](#)] [[INSPIRE](#)].
- [66] P.G.S. Fernandes, C.A.R. Herdeiro, A.M. Pombo, E. Radu and N. Sanchis-Gual, *Spontaneous Scalarisation of Charged Black Holes: Coupling Dependence and Dynamical Features*, *Class. Quant. Grav.* **36** (2019) 134002 [*Erratum ibid.* **37** (2020) 049501] [[arXiv:1902.05079](#)] [[INSPIRE](#)].
- [67] Y. Peng, *Scalarization of horizonless reflecting stars: neutral scalar fields non-minimally coupled to Maxwell fields*, *Phys. Lett. B* **804** (2020) 135372 [[arXiv:1912.11989](#)] [[INSPIRE](#)].
- [68] D.-C. Zou and Y.S. Myung, *Scalarized charged black holes with scalar mass term*, *Phys. Rev. D* **100** (2019) 124055 [[arXiv:1909.11859](#)] [[INSPIRE](#)].
- [69] D. Astefanesei, C. Herdeiro, J. Oliveira and E. Radu, *Higher dimensional black hole scalarization*, *JHEP* **09** (2020) 186 [[arXiv:2007.04153](#)] [[INSPIRE](#)].

- [70] J.L. Blázquez-Salcedo, C.A.R. Herdeiro, J. Kunz, A.M. Pombo and E. Radu, *Einstein-Maxwell-scalar black holes: the hot, the cold and the bald*, *Phys. Lett. B* **806** (2020) 135493 [[arXiv:2002.00963](#)] [[INSPIRE](#)].
- [71] P.G.S. Fernandes, *Einstein-Maxwell-scalar black holes with massive and self-interacting scalar hair*, *Phys. Dark Univ.* **30** (2020) 100716 [[arXiv:2003.01045](#)] [[INSPIRE](#)].
- [72] H. Guo, X.-M. Kuang, E. Papantonopoulos and B. Wang, *Horizon curvature and spacetime structure influences on black hole scalarization*, *Eur. Phys. J. C* **81** (2021) 842 [[arXiv:2012.11844](#)] [[INSPIRE](#)].
- [73] Y.S. Myung and D.-C. Zou, *Scalarized charged black holes in the Einstein-Maxwell-Scalar theory with two U(1) fields*, *Phys. Lett. B* **811** (2020) 135905 [[arXiv:2009.05193](#)] [[INSPIRE](#)].
- [74] Y.S. Myung and D.-C. Zou, *Scalarized black holes in the Einstein-Maxwell-scalar theory with a quasitopological term*, *Phys. Rev. D* **103** (2021) 024010 [[arXiv:2011.09665](#)] [[INSPIRE](#)].
- [75] P. Wang, H. Wu and H. Yang, *Scalarized Einstein-Born-Infeld black holes*, *Phys. Rev. D* **103** (2021) 104012 [[arXiv:2012.01066](#)] [[INSPIRE](#)].
- [76] Q. Gan, P. Wang, H. Wu and H. Yang, *Photon spheres and spherical accretion image of a hairy black hole*, *Phys. Rev. D* **104** (2021) 024003 [[arXiv:2104.08703](#)] [[INSPIRE](#)].
- [77] Q. Gan, P. Wang, H. Wu and H. Yang, *Photon ring and observational appearance of a hairy black hole*, *Phys. Rev. D* **104** (2021) 044049 [[arXiv:2105.11770](#)] [[INSPIRE](#)].
- [78] G. Guo, P. Wang, H. Wu and H. Yang, *Thermodynamics and phase structure of an Einstein-Maxwell-scalar model in extended phase space*, *Phys. Rev. D* **105** (2022) 064069 [[arXiv:2107.04467](#)] [[INSPIRE](#)].
- [79] Y.S. Myung and D.-C. Zou, *Onset of rotating scalarized black holes in Einstein-Chern-Simons-Scalar theory*, *Phys. Lett. B* **814** (2021) 136081 [[arXiv:2012.02375](#)] [[INSPIRE](#)].
- [80] H.-S. Liu, Z.-F. Mai, Y.-Z. Li and H. Lü, *Quasi-topological Electromagnetism: Dark Energy, Dyonic Black Holes, Stable Photon Spheres and Hidden Electromagnetic Duality*, *Sci. China Phys. Mech. Astron.* **63** (2020) 240411 [[arXiv:1907.10876](#)] [[INSPIRE](#)].
- [81] Y. Brihaye and B. Hartmann, *Boson stars and black holes with wavy scalar hair*, *Phys. Rev. D* **105** (2022) 104063 [[arXiv:2112.12830](#)] [[INSPIRE](#)].
- [82] H. Huang, M.-Y. Ou, M.-Y. Lai and H. Lü, *Echoes from classical black holes*, *Phys. Rev. D* **105** (2022) 104049 [[arXiv:2112.14780](#)] [[INSPIRE](#)].
- [83] N.J. Cornish and J.J. Levin, *Lyapunov timescales and black hole binaries*, *Class. Quant. Grav.* **20** (2003) 1649 [[gr-qc/0304056](#)] [[INSPIRE](#)].
- [84] B.F. Schutz and C.M. Will, *Black hole normal modes: a semianalytic approach*, *Astrophys. J. Lett.* **291** (1985) L33 [[INSPIRE](#)].
- [85] B.M. Karnakov and V.P. Krainov, *WKB Approximation in Atomic Physics*, Springer, Berlin Heidelberg, Germany (2013), [[DOI](#)].
- [86] C.M. Bender and S.A. Orszag, *Advanced Mathematical Methods for Scientists and Engineers I*, Springer New York, U.S.A. (1999), [[DOI](#)].